PHYSICAL REVIEW E **103**, 042104 (2021)

Ballistic Brownian motion of supercavitating nanoparticles

Dezhao Huang,[1] Jarrod Schiffbauer,[2] Eungkyu Lee,[3,*] and Tengfei Luo[1,4,*]
[1] *Department of Aerospace and Mechanical Engineering, University of Notre Dame, Notre Dame, Indiana 46556, USA*
[2] *Department of Physical and Environmental Sciences, Colorado Mesa University, Grand Junction, Colorado 81503, USA*
[3] *Department of Electronic Engineering, Kyung Hee University, Yongin-si, Gyeonggi-do, 17104, South Korea*
[4] *Department of Chemical and Biomolecular Engineering, University of Notre Dame, Notre Dame, Indiana 46556, USA*

(Received 16 July 2020; revised 16 December 2020; accepted 9 March 2021; published 5 April 2021)

We show that the Brownian motion of a nanoparticle (NP) can reach a ballistic limit when intensely heated to form supercavitation. As the NP temperature increases, its Brownian motion displays a sharp transition from normal to ballistic diffusion upon the formation of a vapor bubble to encapsulate the NP. Intense heating allows the NP to instantaneously extend the bubble boundary via evaporation, so the NP moves in a low-friction gaseous environment. We find the dynamics of the supercavitating NP is largely determined by the near field effect, i.e., highly localized vapor phase property in the vicinity of the NP.

DOI: 10.1103/PhysRevE.103.042104

I. INTRODUCTION

Brown [1] observed a suspended pollen grain in water undergoing a random walk, and Einstein [2] showed that the mean-squared displacement (MSD) of a particle experiencing such Brownian motion is proportional to the product of its diffusivity and time. When the particle is maintained at a higher temperature than the surrounding fluid, the nonequilibrium temperature field and its induced fluid property (e.g., viscosity) change lead to the so-called hot Brownian motion [3]. Rings *et al.* [3] derived that the apparent diffusivity of the particle experiencing hot Brownian motion can still be described by the Stokes-Einstein relation ($D \propto T/\eta$, where D is the particle diffusion coefficient and the η is the surrounding liquid viscosity), but the temperature and viscosity need to be corrected to consider the nonequilibrium temperature field and the temperature-dependent liquid viscosity. This generalized Stokes-Einstein relation was validated by the measured effective diffusivity of laser-heated gold nanoparticles (NPs) in fluid, where good agreement between theory and measurements was obtained with an excess temperature of the NP up to 150 K. The theoretical framework was further validated using molecular simulations [4,5].

However, when the excitation laser has a power density high enough to form a vapor bubble encapsulating the NP (i.e., supercavitation, Fig. 1), the assumption that temperatures and fluid properties vary continuously is no longer valid due to phase discontinuity. There have been many studies [6–12] on the nanobubble formation around intensely heated NPs. Sasikumar *et al.* [12] used molecular dynamics (MD) to study the cavitation dynamics around such NPs and found that liquid temperature around the NP reached ~90% of the critical temperature. Lombard *et al.* [11] reported the expansion of the nanobubble to be adiabatic by using a hydrodynamic free-energy model. Maheshwari *et al.* [10] determined the exact conditions for the nanobubble formation around a heated NP and found a good agreement with the macroscopic heat balance equation. In these studies, bubble dynamics was the focus with NPs all modeled as fixed particles. Experiments [13] have indeed shown that NPs can be encapsulated by supercavitation upon laser heating at the surface plasmonic resonance, but their Brownian motion, which is expected to be different from hot Brownian motion, has not been studied.

II. METHODS, RESULTS AND DISCUSSION

In this paper, the MD simulation model consists of a NP immersed in a fluid and a solid slab away from the NP as shown in Fig. 1(a), with periodic boundary conditions applied in all directions. For the fluid, the Lennard-Jones (L-J) argon model, $E = 4\varepsilon[(\frac{\sigma}{r})^{12} - (\frac{\sigma}{r})^{6}]$, is used where $\sigma = 3.405$ Å, $\varepsilon_{\mathrm{F-F}} = 0.24\ \mathrm{kcal/mol}$. A time step of 5 fs is used. For the NP, which has a diameter of 1 nm, the Morse potential, $E(r) = D_0[e^{-2\alpha(r-r_0)} - 2e^{-\alpha(r-r_0)}]$, where D_0 is the bond-dissociation energy, r_0 is the equilibrium bond length, and α is the parameter characteristic of the atom, is used with the parameters of $D_0 = 10.954\ \mathrm{kcal/mol}$, $\alpha_{\mathrm{NP}} = 1.583$ Å, $r_{\mathrm{NP}} = 3.042$ Å. The NP interacts with the fluid atoms via the L-J potential with parameters $\sigma_{\mathrm{NP-F}} = 3.405$ Å and $\varepsilon_{\mathrm{NP-F}} = 0.46\ \mathrm{kcal/mol}$ to model the hydrophilic surface. All interactions are truncated at $r_c = 3.67\sigma$. For all simulations, the system is first equilibrated in a canonical ensemble with $T_0 = 0.75\varepsilon/k_{\mathrm{B}}$, and then further equilibrated in an isothermal-isobaric ensemble at the same temperature and pressure of $P = 0.0024\varepsilon/\sigma^3$. The NP is then heated and maintained at T_p ($\geqslant T_0$) by rescaling the thermal velocity of the NP atoms, whereas the center of mass velocity is intact. The slab is maintained at T_0 using a Langevin thermostat to dissipate heat so that the overall temperature of the whole system does not rise constantly. It is worth mentioning that the distance between the NP with the slab is much larger

---

[*] Corresponding authors: eleest@khu.ac.kr; tluo@nd.edu

2470-0045/2021/103(4)/042104(8)

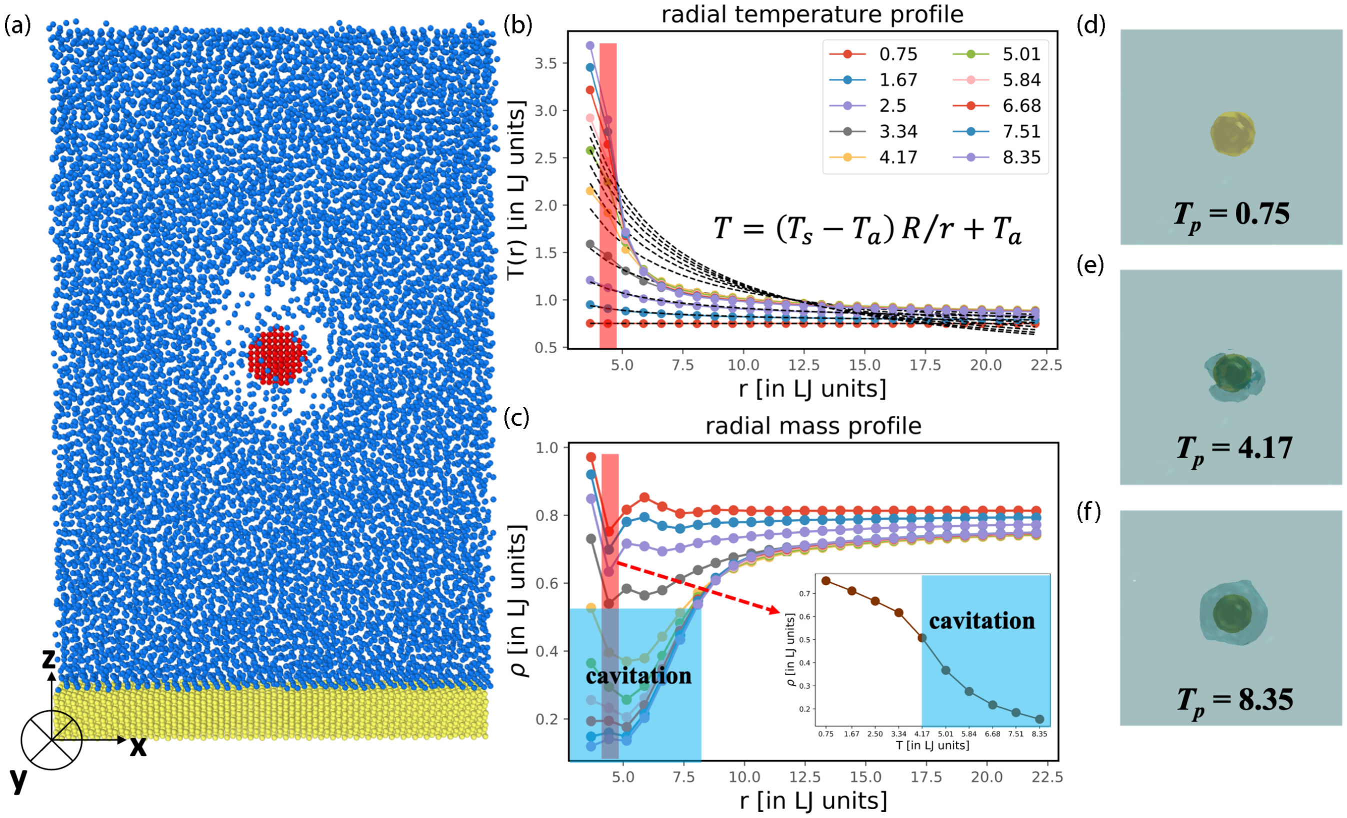

FIG. 1. (a) The simulated structure with a dimension of ~44 × 44 × 73 σ^3; Radial (b) temperature and (c) density profiles of the fluid around the NP maintained at various T_p (the nanoparticle heating temperature). Red shaded regions in (b) and (c) indicate the local temperature and density of fluid in the close vicinity of the NP. Black dotted lines in (b) are the solutions of the heat equation of a heated NP in liquid for the respective T_p conditions. Inset in (c) plots density of the red shaded region as a function of T_p. Color legends are the same for (b) and (c). Blue shaded regions in (c) and its inset are where stable cavitation is observed; (d)–(f) Fluid phase around the heated NP with $T_p = 0.75$, 4.17, and 8.35, respectively. The deeper cyan region indicates the nanobubble generated around the heated NP (see Appendix Note 1 for further details about the visualizations).

than the cutoff, so there is no influence of the slab on the dynamics of the NP. All values reported are in reduced units.

The radial temperature and number density profiles of fluid with the center of NP as the coordinate origin are shown in Figs. 1(b) and 1(c) for cases where the NP is heated to different T_p. More details on implementation and simulations are explained in the Appendix. Supercavitation is apparent when $T_p > 4.17$ as the density in the vicinity of the NP shows a sharp decrease as a function of T_p [inset in Figs. 1(c) and 1(d)–1(f)]. Such findings are consistent with Refs. [12,14]. The existence of the vapor phase can also be inferred by fitting the MD temperature profile using the steady-state heat equation solution in the radial coordinate: $T(r) = (T_s - T_a)R_p/r + T_a$, where T_s is the NP surface temperature, T_a is the ambient liquid temperature, and R_p is the NP radius. The fitted *T(r)* begins to deviate from the MD temperature in the vicinity of the NP when $T_p > 4.17$, suggesting that local thermal conductivity has changed. It is noted that due to the hydrophilic nature of the NP surface, there are always a number of liquid atoms attached to the surface, so the liquid density is not zero right next to the NP even when supercavitation is formed at $T_p = 4.17 \sim 8.35$.

The MSD of the center of mass of NP as a function of time, averaged over 50 independent simulations, for each T_p is shown in Fig. 2(a). MSD increases slowly as T_p increases from 0.75 to 3.34, and an abrupt large increase is seen from $T_p = 3.34$ to $T_p = 4.17$. This threshold coincides with the emergence of supercavitation as indicated in Fig. 1. It is noted that the variation of the MSD curve is large when supercavitation exits, since the NP travel large distances with slower changes in its direction, i.e., the sampling of the phase space is not sufficiently diverse in one simulation [Fig. 2(b)], and that is why large ensemble averaging is needed.

The MSD of Brownian motion generally follows $\langle \text{MSD} \rangle = k_\alpha \Delta t^\alpha$ [20,21], where k_α is the anomalous diffusion coefficient with a unit of $\text{cm}^2\,\text{s}^{-\alpha}$. Depending on α, the dynamics of the NP can be divided into: subdiffusion ($\alpha < 1$)), normal diffusion ($\alpha = 1$), superdiffusion ($1 < \alpha < 2$), and ballistic diffusion ($\alpha = 2$). Figure 2(c) shows that for the isothermal case ($T_p = T_a$), the Brownian NP obeys normal diffusion ($\alpha = 1$). In hot Brownian motion ($T_p > T_a$), but prior to supercavitation, NP exhibits weak superdiffusion ($1 < \alpha < 1.1$). When supercavitation emerges ($T_p \geqslant 4.17$), there is a step increase in α, and it reaches ballistic diffusion ($\alpha = 2$) after $T_p \geqslant 5.01$ at least for times up to the simulation time of 300 ps.

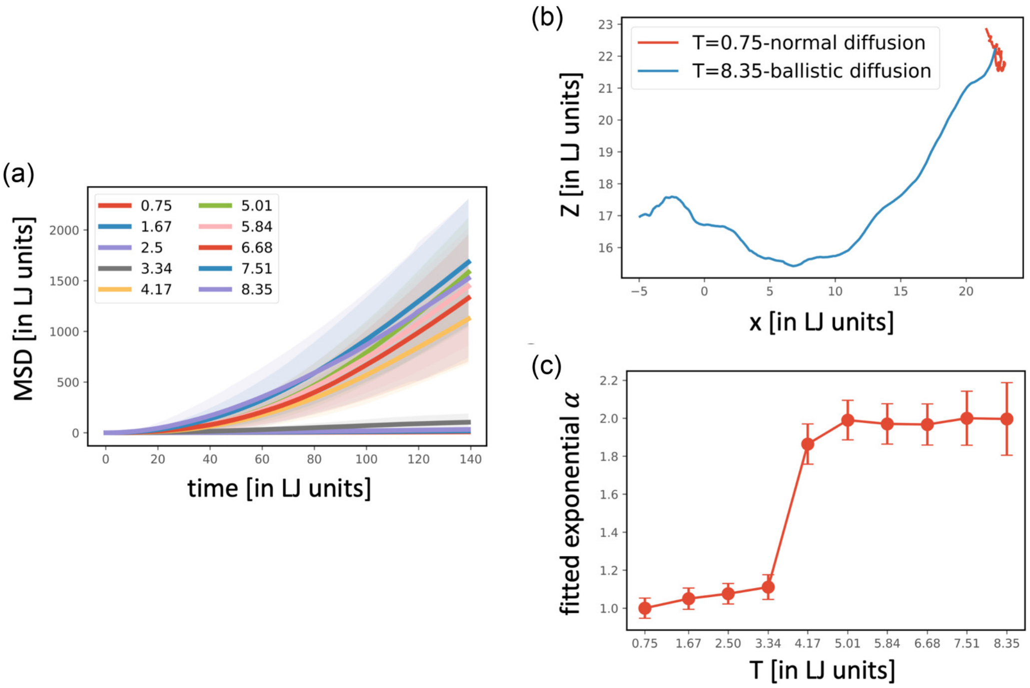

FIG. 2. (a) MSD of the Brownian NP at different T_p. The shaded area represents the standard deviation of the MSD obtained from 50 independent simulations for each T_p. (b) Representative trajectories of NP at $T_p = 0.75$ and 8.35; (c) Fitted exponential α in $\langle MSD \rangle = k_\alpha \Delta t^\alpha$ at different T_p.

Since the anomalous diffusion coefficients, k_α, have different dimensions that depend on α for different T_p, they are not directly comparable. We further calculate the probability density function $f(x,t)$ of the Brownian NP in each dimension using the center of mass positions sampled from 10 independent simulations for each T_p case and averaged the results over all three dimensions [Figs. 3(a) and 3(b)]. We then leverage Eq. (1) to calculate the apparent diffusion coefficient (D) [15]:

$$\frac{\partial f(x,t)}{\partial t} = D\frac{\partial^2 f(x,t)}{\partial x^2}. \tag{1}$$

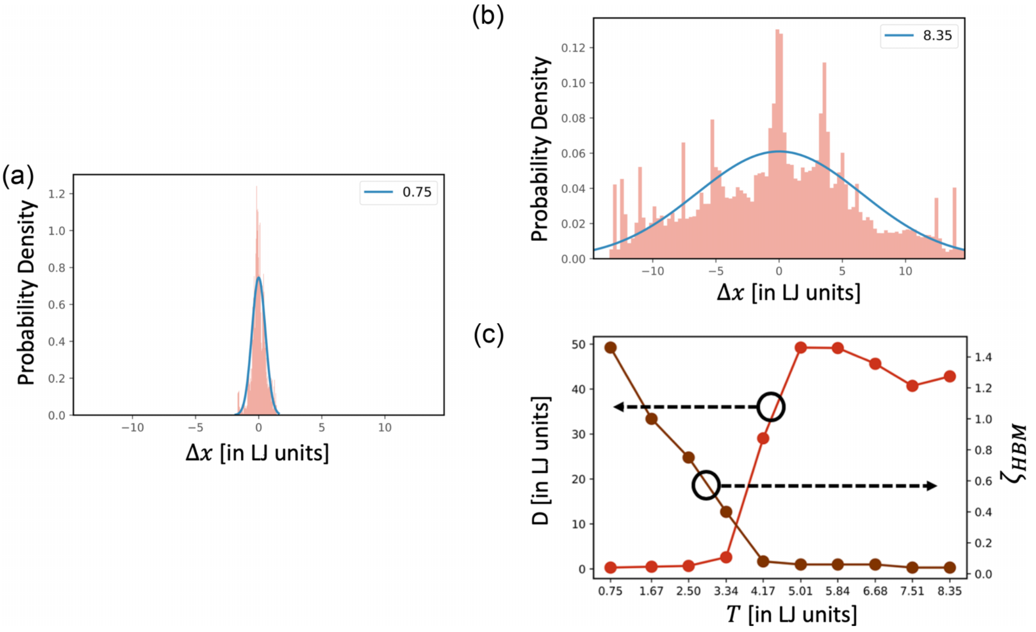

FIG. 3. (a), (b) Selected probability distribution of the NP position for $T_p = 0.75$ and 8.35 (see Fig. 7 in the Appendix for other T_p). Blue curves are the fitted Gaussian distribution; (c) Generalized diffusion coefficient (D) extracted from the NP position probability distribution and apparent friction coefficient (ζ) extracted from the NP velocity autocorrelation function.

The solution to Eq. (1) is a Gaussian function with mean at zero and variance of 2Dt:

$$f(x,t) = \frac{1}{\sqrt{4\pi Dt}} e^{-\frac{(x-u)^2}{4Dt}}. \tag{2}$$

Thus, fitting *f(x,t)* will yield D. We also find that the fitted position mean μ are almost exactly zero for all T_p, which indicates the Brownian nature of NP in all cases. The fitted D increases as T_p increases with a sharp increase from $T_p = 3.34$ to 4.17, coinciding with the onset temperature of supercavitation [Fig. 3(c)]. We also extract the apparent friction coefficient, ζ, from the NP velocity autocorrelation function (see the Appendix, Fig. 5):

$$\langle V(t) \cdot V(0) \rangle = \langle V^2(0) \rangle e^{-(\zeta/m)t}, \tag{3}$$

where m is the NP mass. While ζ decreases gradually prior to supercavitation, a sudden decrease to virtually a frictionless environment for the NP is seen after supercavitation [Fig. 3(c)], supporting the observed ballistic diffusion indicated in Fig. 2(c).

Different from hot Brownian motion [3], which is influenced by the temperature and viscosity field far into the fluid, the observed Brownian motion of the supercavitating NP seems to be dominated by the fluid property local to the bubble. The vapor layer presents large thermal resistance so that the far field temperature is much lower than T_p and is not sensitive to T_p [cases for $T_p > 4.17$ in Fig. 1(b)]. The other important feature is that the high temperature NP can instantaneously evaporate liquid to extend the vapor boundary as it moves, like the Leidenfrost effect [Fig. 4(a)], so that the NP is always enclosed in the vapor environment. This nanoscale Leidenfrost effect was experimentally observed by Lee *et al.* [13], where optical force drives supercavitating NPs to a speed that can only be explained by moving continuously in the gaseous phase. Indeed, in our MD simulations, the velocity of supercavitating Brownian NPs can be as much as 30× higher than that of the normal Brownian motion (see the Appendix, Fig. 8). We note that a similar superfast diffusion phenomenon was also found by Fu *et al.* [16], but in that case, the NP was propelled by a vapor bubble detaching from the NP surface.

As a result, we believe supercavitating Brownian motion is a dominantly near field effect, where for timescales at least on the order of a few hundred picoseconds, the particle moves as a Brownian particle, independent of the fluctuations at the liquid-vapor boundary. To test this hypothesis, we employ a fluctuating hydrodynamics model calculates the effective friction coefficient of a NP at different T_p for a range of physically reasonable far-field conditions using independently obtained simulation data for bulk-like argon (see the Appendix, Note 7 for more details).

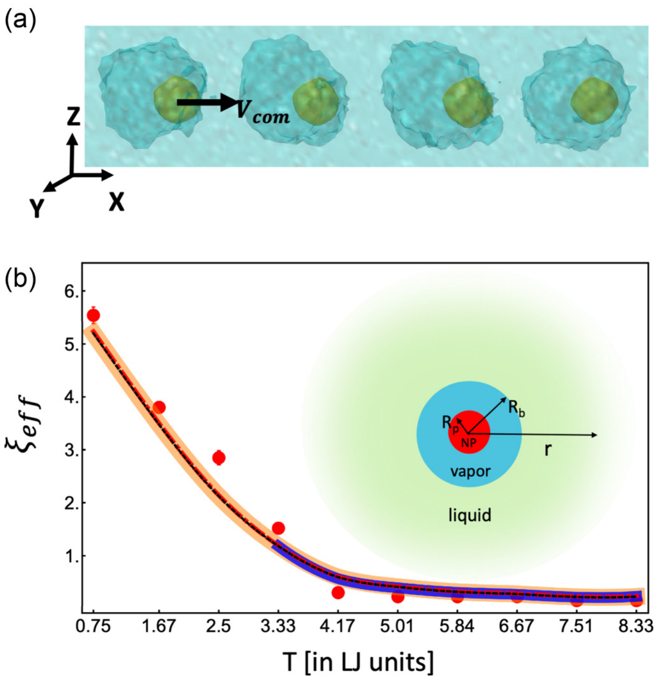

FIG. 4. (a) A representative continuous trajectory of the supercavitating NP at $T_p = 5.01$ showing the bubble boundary is extended outward as the NP moves so it is always encapsulated in a virtually friction environment to achieve ballistic diffusion (see Appendix Note 1 for further details). (b) Comparison between the friction extracted from MD and from the theoretical model. The case for far-field fluid density corresponding to liquid at $T = 0.69$ (black dashed) and $T = 1.24$ (red dashed) show negligible difference from the $T = 0.75$ case (orange solid line). A case with temperature-dependent bubble radius (blue solid line) is shown from $T = 4.5$ to $T = 8.35$. The bubble radius was selected at 7.2σ to get the best fit with the highest temp point for the constant-radius cases and a cubic fit was used for the temperature-dependent radius case. The scattered dots are the friction from the MD simulations. The inset is the schematic illustration of the surrounding environment around the heated NP.

As a first approximation, this model consists of a discontinuous step in density, temperature, viscosity, and pressure corresponding roughly to the respective averages in a low-density, hot vapor bubble region from $r = R_p$ to R_b (R_p is NP radius and R_b is the bubble radius) and the ambient "bulklike" region extending to infinity [see the inset in Fig. 4(b)]. The arguments of Rings *et al.* [5], which critically employ the observations of Keblinskii and Thomin [17] regarding the nature of the fluid velocity fields near NPs, so we replace the actual hydrodynamic velocity field with a much simpler fictitious diffusing scalar field. These arguments permit a straightforward generalization of the original Einstein [2] type of fluctuation-dissipation argument to nonequilibrium situations. Radial symmetry is assumed, and we seek (quasi) steady-state solutions to the spherically symmetric Naiver-Stokes equation (essentially averaging over time dependence and assuming the viscosity $\eta(T)$, density *ρ(T)* and *T* to be spatially uniform)

$$0 = \frac{1}{r^2}\frac{\partial}{\partial r} r^2 \frac{\partial u}{\partial r}. \tag{4}$$

The solution to the above equation represents averages of momentum diffusion over times much longer than the time between a typical molecular collision in the fluid, but shorter than the typical relaxation time of the Brownian motion of the NP.

In the step-bubble model, the velocity field is also taken as steplike. Solutions are sought with a volume-average of zero divergence over the bubble and simultaneously obey mass continuity at the liquid-vapor interface. This assumption is permissible because only the excess heat associated with the frictional motion of the NP is considered. The reaction of the bubble back on the motion of the particle occurs on timescales corresponding to the complete reflection of a pressure wave across the relevant portions of the system. For a bubble of radius ∼1.5 nm and a ∼1-nm radius particle in argon vapor with a speed of sound just over ∼300 m/s, contributions due to fluctuations in the evaporating/condensing boundaries will not affect the effective friction on these time scales. No boundary conditions are imposed on the velocity field at the particle surface, so the solution is in a sense one-sided, like an asymptotic solution. The frictional force is calculated as a reaction force of the NP through the flow to fluctuations in the mechanical pressure, $\xi_{\text{eff}} u(R_p) = -\int P dA$ (i.e., assuming dynamic equilibrium between random hydrodynamic driving and drag forces with similar effective mean field/hydrodynamic character). The effective friction is found by integrating the mechanical pressure from the Navier-Stokes equation over the NP surface so that

$$\xi_{\text{eff}} = -\frac{4\pi R_p^2 \eta(T)}{u(R_p)} \partial_r u|_{r=R_p.} \qquad (5)$$

In each region, well-behaved hydrodynamic solutions are assumed to exist for the flow field. The existence of the far-field solution itself is only required to close the problem at the liquid-vapor boundary, thus accounting for the inertia and momentum of the far field but not coupling its fluctuations to the motion of the NP. Thus, we do not account for the excess heat associated with evaporation and condensation at the liquid-vapor interfaces which the NP, respectively, approaches and recedes since our MD simulations indicate the bubble size to be roughly constant during NP Brownian motion. We emphasize that this is true on time scales comparable to the MD simulations.

In the simple model of the vapor bubble, the temperature, density, and viscosity are taken to be spatially uniform inside the bubble with some effective values to be determined from our definition of the bubble in the MD simulations. The solutions are denoted u and u' in the vapor and liquid regions, respectively. Even though we assume the bubble has an average density, the vapor layer solution need not obey the incompressibility condition. Thus, we may use the solution $u(r) = a_0 + \frac{a_1}{r}$. However, incompressibility is imposed on average over the volume of the bubble, including both the liquid and vapor sides of a (nonequilibrium) Gibbs-like nonequilibrium phase boundary. Thus, imposing that the volume integral of $\nabla \cdot u$ is zero over the whole bubble couples the two solutions to guarantee the flow field corresponds to the correct average force balance acting on the NP in the absence of coupling to far-field fluctuations (i.e., the actual fluctuating liquid-vapor boundary.) Applying the divergence theorem to the integral of the velocity divergence over a spherical shell corresponding to the vapor bubble then permits a matching relationship of $R_p^2 u(R_p) = R_b^2 u'(R_b)$. Continuity of mass flux at the bubble boundary requires that $\rho_V u(R_b) = \rho_L u'(R_b)$. By defining $\phi(T) = \rho_v(T)/\rho_L$ and $\alpha(T) = R_b/R_p$, the coefficients for $u(r)$ may be related via $a_0 = a_1 \frac{1}{R_p} \frac{(\phi-\alpha)}{(\alpha^2-\phi)}$, and the calculated friction coefficient is $\xi_{\text{eff}}(T) = 4\pi \eta(T) R_p \frac{\alpha^2(T)-\phi(T)}{\alpha^2(T)-\alpha(T)}$. Note that the far-field density, ρ_L, essentially plays the role of a normalization constant in the mass continuity at the liquid-vapor interface. Since the definition of the liquid-vapor boundary on these length scales is somewhat subjective [see Fig. 1(c)], which is implicit in our above imposition of a nonequilibrium Gibbs dividing plane, we choose to leave the bubble radius as a free parameter. This is also consistent with our hypothesis regarding relative independence of far-field conditions. There is weak dependence on the bubble radius for the regime of interest, above the cavitation threshold. Below this, a more correct theoretical description would require more careful treatment of the viscosity and temperature profiles, a la Rings *et al.* [3,5].

To calculate $\xi_{\text{eff}}(T)$ for each T_p case, we take $\rho_v(T_p)$ as the effective fluid density in the vicinity of the NP from the respective MD simulations [red shaded region in Fig. 1(c)].

We then performed isothermal MD simulations on bulk argon fluid with temperatures and densities equal to the effective values in the vicinity of the NP for each T_p case [red shaded regions in Figs. 1(b) and 1(c)] to calculate its shear viscosity using the Green-Kubo relationship (see the Appendix, Fig. 6), which are then used as $\eta(T_p)$ in the hydrodynamic model. The model is then used to reproduce the MD-calculated friction coefficients with the bubble radius being the only adjusting parameter.

As seen in Fig. 4(b), the model agrees well with the MD data between $T_p = 4.17$ and 8.35, when using $R_b = 7.2\,\sigma$ which is in the same range as the bubble radii in MD. The small difference may be mainly attributed to the definition of vapor phase in MD, which is somewhat subjective, as is the actual bubble radius, and the simplification of the step-bubble profile in the hydrodynamic model which does not account for local gradients (known to shift the effective friction [3]. This may contribute to the difference between the MD simulations and the model especially in the range $T_p = 4$ to $T_p = 5$ (bubble nucleation). We tested the influence of liquid property change and overall bubble radius on ξ_{eff} using the model, but virtually no change in ξ_{eff} is observed [Fig. 4(b)] for realistic changes in fluid density nor is there any strong dependence on the bubble radius for reasonable bubble sizes. It is worth noting that the agreement between the results obtained from simulations and the model using independent data and a piecewise-defined bubble does verify our assumption and the variation of the far-field properties across the widest physically sensible range produces no appreciable difference in the effective friction. While the far-field fluid conditions enter into the calculation of effective friction to ensure conservation laws are satisfied, for reasonable fluid densities, most of the dependence of the effective friction on the temperature is determined by the changes in the near-field quantities. Together, these strongly suggest that the supercavitation makes NP Brownian motion a near field effect. Without supercavitation, ξ_{eff} varies strongly as liquid property changes [Fig. 4(b)].

III. CONCLUSION

Although our model does not directly correspond to a realistic system, the developed hydrodynamics model which is validated against MD results can be used to predict a realistic situation. We further collected the experimental NP/nanobubble relevant data from Lee *et al.* [13] and used our hydrodynamic model to predict the effective viscosity of the liquid/gas environment around the ballistic gold NP. For example, for a 60-nm radius NP and a 90-nm radius generated nanobubble, our hydrodynamic model-predicted effective viscosity is around 5.9×10^{-5} Pa S, which is approximately two times larger than the water vapor viscosity ($\sim 2.97 \times 10^{-5}$ Pa S) [18] and four times smaller than the liquid state viscosity ($\sim 2.3 \times 10^{-4}$ Pa S) [18]. Our observed ballistic NPs encapsulated in a bubble is indeed similar (in order of magnitude) to the Brownian motion in the vapor situation since the phase change at the liquid-vapor interface is not important due to the instantaneously evaporating phenomena, which ensures the NP is constantly encapsulated in the vapor phase. It is also worth noting that varying the bubble size would not change the order of the magnitude of the effective viscosity we predicted for a range of reasonable bubble radius from 90 to 250 nm in the experiment although the bubble diameter depends on the laser fluence. Our developed hydrodynamic model predicts that the effective viscosity of a supercavitating Brownian gold NP would be much smaller than that in the pure liquid phase, which may be potentially measured in the future.

ACKNOWLEDGMENTS

D.H. acknowledges financial support from the Chinese Scholarship Council. T.Z., E.L., and T.L. are thankful for the support from the National Science Foundation (NSF) (Grants No. 1706039 and No. 1937923), the Center for the Advancement of Science in Space (Grant No. GA-2018-268), and the Dorini Family for the endowed professorship in Energy Studies. The simulations are supported by the Notre Dame Center for Research Computing, and NSF through XSEDE computing resources provided by SDSC Comet and Comet and TACC Stampede under Grant No. TG-CTS100078.

D.H. performed all MD simulations and formal analyses. J.S. derived the hydrodynamics model. All authors discussed the results and the mechanism of the ballistic Brownian motion of supercavitating nanoparticles. D.H., J.S., E.L and T.L. wrote the manuscript.

APPENDIX: MATERIALS AND METHODS

1. Three-dimensional meshing to visualize the vapor boundary

To further illustrate the movement of the heated NP inside the nanobubble at the molecular level, we divide the whole liquid region into a fine three-dimensional grid. Each unit domain is of size $\sim \sigma\ (y)\ \times \sigma\ (y) \times \sigma\ (z)$. By calculating mass density at each domain, we are able to distinguish the liquid/vapor boundary and found that the hot NP can constantly evaporate liquid while moving and keeps pushing the vapor boundary during the fast movement as shown Figs. 1(d)–1(f) and 4(a). Here the bubble interface location is determined by half of the ambient liquid density [12,14]. A nanobubble is considered to be formed when the fluid/gas density is below half of the ambient liquid density.

2. Center of mass velocity autocorrelation function

The center of mass velocity autocorrelation of the nanoparticles with different heating temperatures were calculated using the ensemble average.

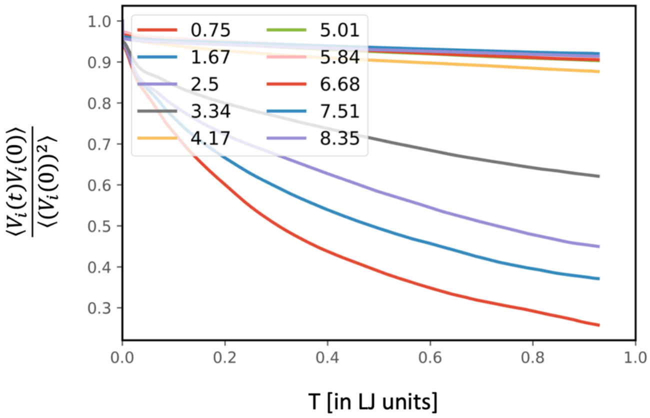

FIG. 5. Center of mass velocity autocorrelation as a function of different nanoparticle heating temperatures.

3. Shear viscosity of pure argon at valley temperature and density

The shear viscosity of the surrounding liquid/gas for nanoparticles is calculated using the density and temperature from the first valley point from radial temperature and mass density profile [the shaded regions in Figs. 1(b) and 1(c)].

See Fig. 6 below.

4. Probability distribution of the NP position at different temperatures

See Fig. 7 below.

5. Steady state nanobubble radius from $T_p = 4.17$ to T_p to 8.35.

See Table I below.

6. The normalized mean NP velocity at different T_p

See Fig. 8 below.

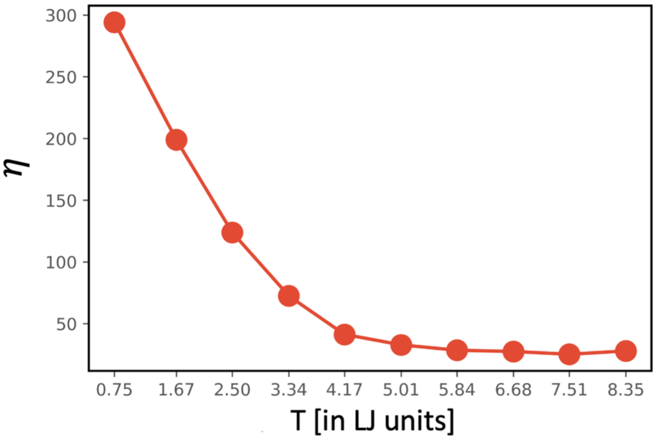

FIG. 6. The shear viscosity of pure argon liquid/gas at valley temperature and density conditions.

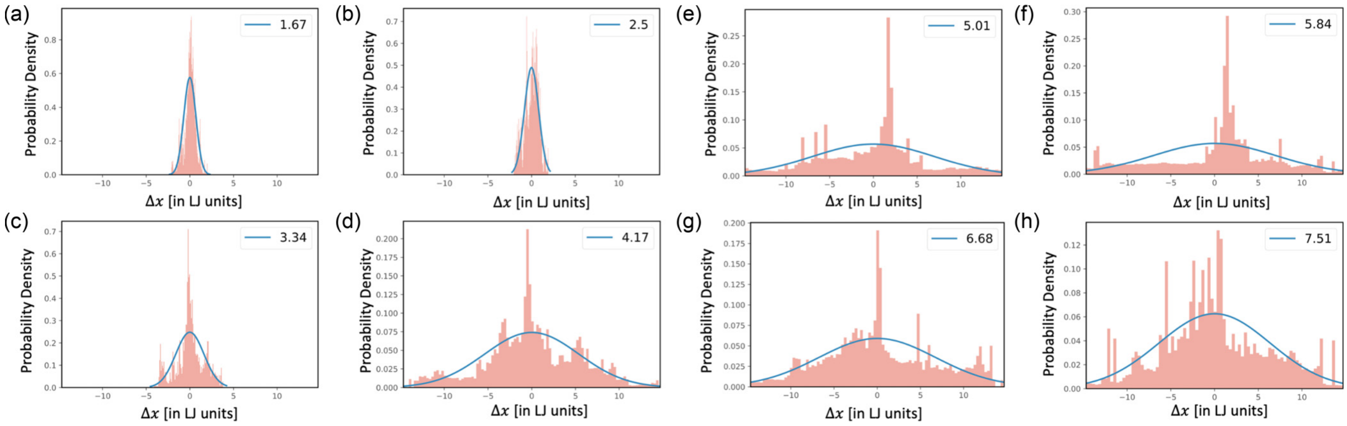

FIG. 7. The position probability density function of the heated Brownian NP for $T_p = 1.67$ to $T_p = 7.51$.

7. Details and discussions on the hydrodynamic model

For a mesoscale hydrodynamics model defined over a nanoscale vapor volume, we will seek an effective solution for a fictitious time-averaged flow velocity with purely radial symmetry in the spirit of Rings *et al.* [3]. For simplicity, we assume this is the only spatially nonuniform field within the bubble and introduce effective average temperatures and densities with a step at the liquid-vapor interface. A more accurate model would include all gradient contributions, including the density gradient, which captures effects of condensation and evaporation [19]. But this is not necessary for the present purpose, which is principally to examine the dependence of such ballistic Brownian motion on near-field vs far-field properties.

We take a solution of the spherical Naiver-Stokes equation, which is bounded at infinity, $u(r) = a_0 + \frac{a_1}{r}$, and assume there may be different solutions u and u' in the vapor and liquid regions. However, it turns out that the solution in this 'outer' liquid region is not needed explicitly because it can be eliminated from the problem outside of bookkeeping at the liquid-vapor boundary (the nanoparticle excludes the singularity at $r = 0$.) We only impose a boundary condition at the liquid-vapor interface, namely mass continuity per unit volume, or $\rho_V u(R_b) = \rho_L u'(R_b)$. Thus, the solution is one-sided in the spirit of an asymptotic solution. In disposing of the angular portion of the (quasisteady) flow, we are in effect taking both time and volume averages to define *u(r)*. Therefore, we will only require that the average over many molecular collisions provide the required force on the particle, i.e., corresponding to the Brownian motion, through the integral of the mechanical pressure over the particle surface. Taking the (dynamic) equilibrium between hydrodynamic drag and pressure, Newton's law yields, $\xi_{\text{eff}} u(R_p) = -\int P dA$. This enables us to calculate the effective friction, again simply following Rings [3]. The mechanical pressure at the particle surface is given by $P = \eta(T)\partial_r u|_{r=R_p}$.

TABLE I. The steady state nanobubble radius at $T_p = 4.17$ to $T_p = 8.35$.

Temperature (in LJ unit)	4.17	5.01	5.84	6.68	7.51	8.35
Radius (A)	21.5	23.3	23.7	24.0	24.4	24.6

We require one more assumption to close the problem. In assuming a steplike bubble, excepting the effective momentum diffusion (flow) field *u(r)*, we are dealing with spatially uniform quantities which represent effective (average) local quantities. Therefore, even though we do not impose incompressibility on the flow (strictly speaking, the vapor need not obey incompressibility at all,) we instead impose the following condition: the *volume average* of the flow field is incompressible, i.e., the *average* density remains constant at fixed temperature during a virtual deformation of the bubble corresponding to motion of the NP,

$$\frac{1}{4\pi R^3}\int_{\text{Volume}} \nabla \cdot u d\Omega = 0. \tag{A1}$$

Applying the divergence theorem, the integral is transformed into a surface integral evaluated at the particle-vapor and vapor-liquid interfaces respectively, or,

$$\tfrac{4}{3}\pi R_p^2 u(R_p) = \tfrac{4}{3}\pi R_b^2 u^{'(R_b)}. \tag{A2}$$

Temperature-dependent density $\phi(T) = \rho_v(T)/\rho_L$ and radius ratios $\alpha(T) = R_b/R_p$ are introduced. The coefficients may be related

$$a_0 = a_1 \frac{1}{R_p}\frac{(\phi - \alpha)}{(\alpha^2 - \phi)}, \tag{A3}$$

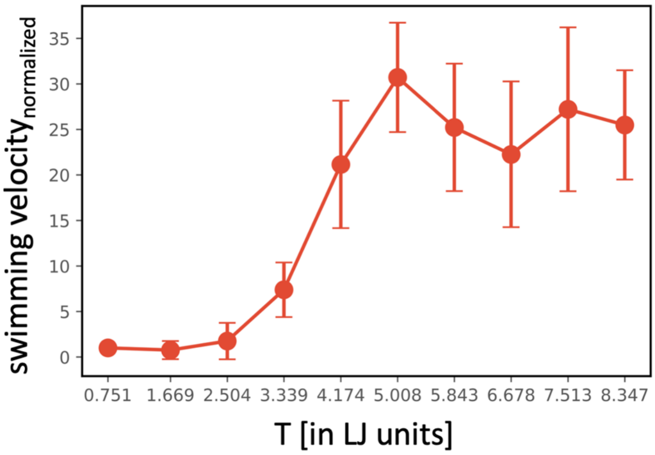

FIG. 8. The normalized mean NP velocity at different T_p.

so that the effective friction may be solved in terms of temperature-dependent (bulk) data obtained from independent MD simulations along with the temperature-dependent bubble radius. The model, however, is relatively insensitive to the temperature-dependence of the bubble radius (for physically reasonable radii.) This again emphasizes that principally the local quantities determine the dynamics.

---

[1] P. Pearle, B. Collett, K. Bart, D. Bilderback, D. Newman, and S. Samuels, What Brown saw and you can too, Am. J. Phys. **78**, 1278 (2010).

[2] A. Einstein, Zur theorie der Brownschen bewegung, Ann. Phys. Lpz. **324**, 371 (1906).

[3] D. Rings, R. Schachoff, M. Selmke, F. Cichos, and K. Kroy, Hot Brownian Motion, Phys. Rev. Lett. **105**, 090604 (2010).

[4] D. Chakraborty, M. V. Gnann, D. Rings, J. Glaser, F. Otto, F. Cichos, and K. Kroy, Generalized Einstein relation for hot Brownian motion, EPL **96**, 60009 (2011).

[5] D. Rings, M. Selmke, F. Cichos, and K. Kroy, Theory of hot Brownian motion, Soft Matter **7**, 3441 (2011).

[6] R. Angélil, J. Diemand, K. K. Tanaka, and H. Tanaka, Bubble evolution and properties in homogeneous nucleation simulations, Phys. Rev. E **90**, 063301 (2014).

[7] Y. Chen, Y. Zou, Y. Wang, D. Han, and B. Yu, Bubble nucleation on various surfaces with inhomogeneous interface wettability based on molecular dynamics simulation, Int. Commun. Heat Mass Transfer **98**, 135 (2018).

[8] B. Li, Y. Gu, and M. Chen, Cavitation inception of water with solid nanoparticles: A molecular dynamics study, Ultrason. Sonochem. **51**, 120 (2019).

[9] S. Merabia, P. Keblinski, L. Joly, L. J. Lewis, and J.-L. Barrat, Critical heat flux around strongly heated nanoparticles, Phys. Rev. E **79**, 021404 (2009).

[10] S. Maheshwari, M. van der Hoef, A. Prosperetti, and D. Lohse, Dynamics of formation of a vapor nanobubble around a heated nanoparticle, J. Chem. Phys. C **122**, 20571 (2018).

[11] J. Lombard, T. Biben, and S. Merabia, Kinetics of Nanobubble Generation Around Overheated Nanoparticles, Phys. Rev. Lett. **112**, 105701 (2014).

[12] K. Sasikumar and P. Keblinski, Molecular dynamics investigation of nanoscale cavitation dynamics, J. Chem. Phys. **141**, 234508 (2014).

[13] E. Lee, D. Huang, and T. Luo, Ballistic supercavitating nanoparticles driven by single Gaussian beam optical pushing and pulling forces, Nat. Commun. **11**, 2404 (2020).

[14] J. H. Pu, J. Sun, W. Wang, and H. S. Wang, Generation and evolution of nanobubbles on heated nanoparticles: A molecular dynamics study, Langmuir **36**, 2375 (2020).

[15] X. Bian, C. Kim, and G. E. Karniadakis, 111 years of Brownian motion, Soft Matter **12**, 6331 (2016).

[16] X. Fu, B. Chen, J. Tang, and A. H. Zewail, Photoinduced nanobubble-driven superfast diffusion of nanoparticles imaged by 4D electron microscopy, Sci. Adv. **3**, e1701160 (2017).

[17] P. Keblinski and J. Thomin, Hydrodynamic field around a Brownian particle, Phys. Rev. E **73**, 010502(R) (2006).

[18] P. Linstrom, NIST chemistry webbook, NIST Standard Reference Database 69, https://doi.org/10.18434/T4D303.

[19] J. Schiffbauer and T. Luo, Liquid phase stabilization versus bubble formation at a nanoscale curved interface, Phys. Rev. E **97**, 033106 (2018).

[20] J. R. Gomez-Solano and F. J. Sevilla, Active particles with fractional rotational brownian motion, J. Stat. Mech. (2020) 063213.

[21] J.-H. Jeon and R. Metzler, Fractional Brownian motion and motion governed by the fractional Langevin equation in confined geometries, Phys. Rev. E **81**, 021103 (2010).